Microstructural Evolution of Ni-SiC Composites Manufactured by Spark Plasma Sintering

MARCIN CHMIELEWSKI, RAFAŁ ZYBAŁA, AGATA STROJNY-NĘDZA, ANNA PIĄTKOWSKA, ARTUR DOBROWOLSKI, JAKUB JAGIEŁŁO, RYSZARD DIDUSZKO, PIOTR BAZARNIK, and SZYMON NOSEWICZ

The presented paper concerns the technological aspects of the interface evolution in the nickel-silicon carbide composite during the sintering process. The goal of our investigation was to analyse the material changes occurring due to the violent reaction between nickel and silicon carbide at elevated temperatures. The nickel matrix composite with 20 vol pct SiC particles as the reinforcing phase was fabricated by the spark plasma sintering technique. The sintering tests were conducted with variable process conditions (temperature, time, and pressure). It was revealed that the strong interaction between the individual components and the scale of the observed changes depends on the sintering parameters. To identify the microstructural evolution, scanning electron microscopy, energy dispersive spectroscopy, transmission electron microscopy, X-ray diffraction, and Raman spectroscopy were used. The silicon carbide decomposition process progresses with the extension of the sintering time. As the final product of the observed reaction, new phases from the Ni-Si system and free carbon were detected. The step-by-step materials evolution allowed us to reveal the course of the reaction and the creation of the new structure, especially in the reaction zone. The detailed analysis of the SiC decomposition and formation of new components was the main achievement of the presented paper.

I. INTRODUCTION

SILICON carbide (SiC), due to its unique properties, seems to be one of the most promising materials for modern applications. Due to its wide band gap value, high breakdown electric field, good thermal and electrical conductivity, and high hardness and mechanical strength, SiC can be applied in the electronic (*e.g.*, high power/high frequency devices) or automotive (*e.g.*, brake discs) industry.[1] Silicon carbide is also used as the reinforcement in metal,[2–8] ceramic,[9,10] or polymer matrix composites.[11,12] SiC addition can improve the thermal or mechanical properties,[13] especially in the case of metal matrix composites.

The group of nickel matrix composites is of special interest. There are many works dedicated to the manufacturing and characterization of Ni-SiC composites in the form of coatings[14–17] and bulk materials.[18–20]

The pulse electrodeposition technique is the most commonly used for the fabrication of nickel-based composite coatings. In the case of layered systems nanoparticles of silicon carbide are typically used[18,21,22] which is justified due to the low thickness of the coating. For thin films, the possible reactions depend on the relative amounts of Ni and Si available for the mutual interaction, the process temperature and atmosphere, and the impurities contained in the layers. Low processing temperature (electroforming) or short time of high-temperature exposure (laser deposition) can strongly limit or even exclude the interfacial reaction in opposition to the sintered materials.

For the synthesis of Ni-SiC in the bulk form, powder metallurgy methods can be applied. No data about Ni-SiC composites obtained *via* the spark plasma sintering method can be found in the literature. The main technological problem of obtaining Ni-SiC

MARCIN CHMIELEWSKI is with the Lukasiewicz Research Network, Institute of Microelectronics and Photonics, Center of Functional Materials, 133 Wolczynska Str, Warsaw, Poland and also with the National Centre for Nuclear Research, 7 Soltana Str, 05-400, Otwock, Poland. RAFAŁ ZYBAŁA, AGATA STROJNY-NĘDZA, ANNA PIĄTKOWSKA, ARTUR DOBROWOLSKI, JAKUB JAGIEŁŁO, RYSZARD DIDUSZKO are with the Lukasiewicz Research Network, Institute of Microelectronics and Photonics, Center of Functional Materials, 133 Wolczynska Str, Warsaw, Poland. PIOTR BAZARNIK is with the Warsaw University of Technology, 141 Wołoska Str, 02-507, Warsaw, Poland. SZYMON NOSEWICZ is with the Institute of Fundamental Technological Research, Polish Academy of Sciences, 5B Pawinskiego, 02-106, Warsaw, Poland. Contact e-mail: snosew@ippt.pan.pl

composites is the mutual reactivity of the components of the composite occurring at elevated temperatures. At temperatures exceeding 500 °C, nickel reacts with silicon carbide, which causes SiC decomposition and the creation of pure components (Si and C).[23] As a result, free carbon is precipitated and silicon interacts with nickel, forming new Ni-Si phases. Based on the equilibrium phase diagram, nine Ni-Si compounds can be distinguished, *e.g.,* Ni_3Si, $Ni_{31}Si_{12}$, Ni_2Si, Ni_3Si_2, $NiSi$, and $NiSi_2$. The authors of[24] indicated that individual Ni-Si phases are formed as a result of melting and casting and the solid-state reaction between Ni and Si.

In the case of sintering materials showing mutual solubility, intermediate phases with varying component concentrations may appear at particular stages of the densification process. In such a case, the free energy of the sintered system is decreased not only as a result of the reduction of the pore surface area but also as a result of mutual diffusion contributing to the alignment of the material composition or leading to the formation of stable intermediate phases.[25] Several papers analyzing the Ni-SiC behavior at elevated temperatures can be found in the literature.[26–30] The investigations mainly concern the post-manufacturing thermal treatment of Ni-SiC systems and its effect on the structural evolution and physical properties. There are many sophisticated experimental tools applied to describe the correlation between the material structure, microstructure, and properties *vs.* temperature. For example, the authors of[14] examined the influence of the heat treatment on the tensile strength of the Ni-SiC composite. The almost 50 pct increase in the maximum strength was obtained for materials annealed in a vacuum for 24 hours at 300 °C compared to the reference sample. The increase in the temperature to 600 °C caused the drastic decrease in the material strength. It was explained by the interfacial reaction and formation of new compounds (Ni_3Si and a little amount of $Ni_{31}Si_{12}$) and a change in the fracture mechanisms of the material. In,[31] the interfacial interaction and phase changes occurring during heating (600 °C to 1000 °C) of the nickel thin film deposited on the 6H-SiC substrate were examined. Based on the ternary diagram (Figure 1), it was stated that only the Ni_2Si

phase was identified between 600 °C and 950 °C. Additionally, the free carbon, as the product of SiC decomposition, occurs in the structure in the form of precipitates.

Available literature data indicated how many technological factors influence the material composition. Additionally, the type (understood as shape, morphology and particle size) of starting materials and the method of densification can affect the behavior of the material during sintering. The knowledge of the fundamental phenomena occurring in the material's structure during the densification process has a crucial role in designing new materials solutions. This is of great importance in the case of newly developed technologies, such as SPS, with high application potential.

The authors of[23] presented the calculation of the Gibbs free energies for different possible reactions in the Ni-Si-C system. It was stated that due to the strong affinity between Si and Ni and the strong Si-C bond, the formation of nickel silicades is possible only at elevated temperatures when the thermal energy can overcome the activation barrier.

Our work seems to be the first attempt to analyze the relationship between the SPS sintering condition and microstructural changes in the Ni-SiC bulk composite. Special attention was paid to the metal-ceramic interface, responsible for the quality of composite materials. The samples were sintered by the spark plasma sintering (SPS) method, allowing for relatively quick densification in conditions of limited temperature compared to conventional sintering.[30] In the SPS method, direct electric current flow is a heating source for sintering of powder material. Additionally, application of a uniaxial mechanical load supports the diffusion processes, allowing for material densification. Our motivation was to determine the influence of the temperature, sintering time, electric current, and mechanical load on the course of changes in the structure of the sintered Ni-SiC material. It should be emphasized that the performed investigation is the first original analysis dedicated to the manufacturing of Ni-SiC composites *via* the Spark Plasma Sintering method. Obtained results seem to be a good reference for researchers using SPS for the manufacturing of advanced materials.
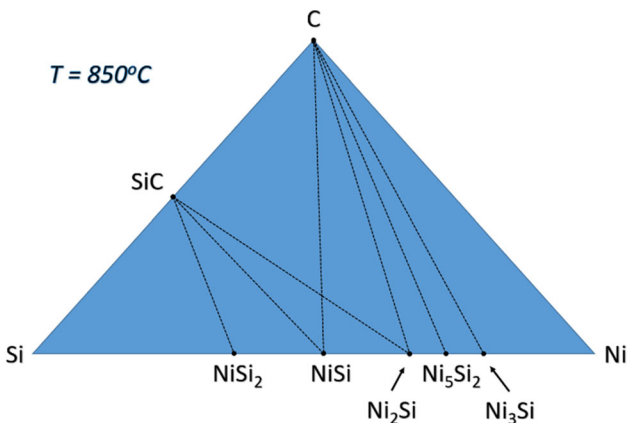
II. MATERIALS AND METHODS

Ni-SiC composites were prepared *via* the powder metallurgy route. For the starting material, nickel powder (NewMet Koch, 5 μm, 99.9 pct) and SiC powders (Saint-Gobin, 80 μm, 99.99 pct) were selected as the matrix and the reinforcement, respectively. The morphology of the starting powders is presented in Figure 2.

In order to provide a uniform distribution of elements in the powder mixture, the mixing process was conducted in a planetary ball mill (Pulverisette 6, Fritsch). A nickel-based composite mixture containing 20 vol pct silicon carbide was prepared in the tungsten carbide (WC)/cobalt (Co) container using the following mixing parameters: rotational speed ω = 100 rpm, mixing time
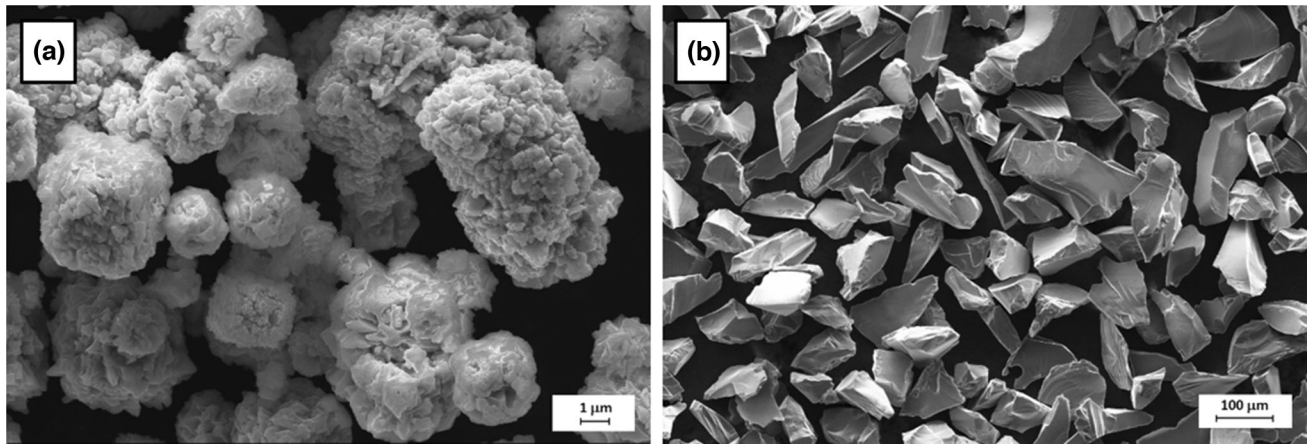

Fig. 1—Ternary phase diagrams of Ni-Si-C at 850 °C.[31]

Fig. 2—Materials used in the experiment: (*a*) nickel and (*b*) silicon carbide.

Table I. Sintering Condition of Nickel-Based Materials

Material	Sintering temperature (°C)	Sintering time (minutes)	External pressure (MPa)
Ni-20SiC (Sample 1)	850	1	50
Ni-20SiC (Sample 2)	850	5	50
Ni-20SiC (Sample 3)	850	15	50
Ni-20SiC (Sample 4)	850	30	50
Ni-20SiC (Sample 5)	850	5	5
Ni-20SiC (Sample 6)	1000	5	50
Pure nickel (Sample 7)	850	5	50

t = 4 hours, ball-to-powder ratio = 5:1, WC/Co milling balls—10 mm in diameter. The densification process was provided in the SPS apparatus. The sintering conditions are presented in Table I. The process conditions were selected based on the preliminary sintering tests for pure nickel (Sample 7), assuming a high densification rate of the obtained samples. The system was heated at a rate of 100 °C/minute to 700 °C (800 °C in the case of Sample 6), and then the heating rate was slowed down to 50 °C until the desired sintering temperature was reached. After the holding time, the samples were naturally cooled to room temperature with an average cooling rate of 10 °C/minute. The external load was released from 50 to 0 MPa directly after the desired holding time. The diversification of the process parameters was conditioned by obtaining a different degree of interaction between the components of the composite.

The Ni-SiC composites were sintered in graphite die and punches. As a result, samples of 25 mm in diameter were obtained. As received materials were cut, ground, and polished for further investigations. The density of the Ni-SiC composites was measured using the hydrostatic method based on Archimedes' principle. Additionally, the relative density ρ_{rel} was determined as the ratio of the measured bulk density ρ_m and the theoretical density ρ_t of the Ni-SiC composite. For calculations, the density of Ni and SiC was assumed to be ρ_{Ni} = 8.9 g/cm^3 and ρ_{SiC} = 3.2 g/cm^3, respectively.

Next, the detailed microstructural analysis including scanning electron microscopy with energy dispersive spectroscopy and transmission electron microscopy was performed. The machined surface (ground and polished) of the samples was analysed using the scanning electron microscope Auriga produced by the Zeiss company (Oberkochen, Germany). The detailed microstructural observations of the interface forming between the Ni matrix and SiC particles were carried out on a high resolution scanning transmission electron microscope (STEM) Hitachi HD-2700 operating under an accelerating voltage of 200 kV. Structural investigations were combined with advanced energy dispersive X-ray (EDX) point and mapping analyses. The selected area electron diffraction (SAED) patterns were taken using a transmission electron microscope (TEM) JEOL JEM-1200EX. Thin foils with a thickness of ~ 100 nm for STEM and TEM investigations were prepared by the focused ion beam (FIB) lift-out technique using a FIB-SEM Hitachi NB5000 system.

The structural changes were analysed using X-ray diffraction and Raman spectroscopy. *Ex-situ* X-ray powder diffraction measurements were performed using the Rigaku SmartLab 3 kW diffractometer equipped with a high-speed 1D silicon strip detector D/teX Ultra 250 and filtered Cu K$_\alpha$ radiation. The powder diffraction patterns were measured in the $\theta/2\theta$ Bragg–Brentano geometry in the angular range of $10° \leq 2\theta \leq 100°$ with a scanning step of 0.01° and a speed of 2°/minute.

Table II. Density Results of the Sintered Ni-SiC Composites

Material	Theoretical density (g/cm^3)	Measured density (g/cm^3)	Relative density (percent)
Ni-20SiC (Sample 1)	7.76	7.29	93.9
Ni-20SiC (Sample 2)		7.48	96.4
Ni-20SiC (Sample 3)		7.56	97.4
Ni-20SiC (Sample 4)		7.71	99.4
Ni-20SiC (Sample 5)		6.13	79.0
Ni-20SiC (Sample 6)		7.59	97.3
Pure Nickel	8.90	8.65	97.2

Qualitative analysis was performed using a database PDF-4 + 2021 and the Integrated X-ray Powder Diffraction Software PDXL2 supplied by Rigaku. Experimental data were also analyzed using the quantitative Rietveld refinement method using the PDXL2 software.

Additional information on the composition of the material inside the particles was obtained by performing Raman spectroscopy measurements with a Renishaw spectrometer using a 532 nm (2.33 eV) Nd:YAG laser and an Andor Newton CCD detector. The laser beam was focused using a lens with 100 times magnification. The system allowed spectra to be collected in the spectral range from 0 to 2800 cm^{-1} from the areas of interest.

III. RESULTS

A. *Physical Properties*

The results of the Ni-SiC density measurements are presented in Table II. The densification degree increases with the holding time at a sintering temperature of 850 °C. Application of a lower external pressure (5 MPa) results in a significant amount of residual porosity in comparison to the composite sintered with a higher load. In contrast, for Sample 6 sintered at 1000 °C, an almost fully dense composite is obtained in a shorter sintering time.

B. *X-Ray Diffractometry*

X-ray diffraction patterns for selected Ni-SiC composite materials in comparison to the starting powder mixture are presented in Figure 3. According to Figure 3(a), the starting material for sintering was a mixture of Ni powder with cubic structure (fcc) and SiC silicon carbide—polytype 6H without visible impurities. With the sintering progress, the observed phase changes resulting from the interaction at the metal-ceramic interface were identified [Figure 3(b)]. First, small phase changes can be observed for Sample 1 (850 °C, 1 minute). Despite the short exposure time at an elevated temperature, three peaks (for 2θ angles approx. 45°, 47°, 67°) of the newly formed $Ni_{31}Si_{12}$ phase were identified. Extension of the sintering time of the composite material of up to 5 minutes (Sample 2—red curve) caused the increase in the peak intensity, which proves the

progressive decomposition of silicon carbide and the increase in the amount of the $Ni_{31}Si_{12}$ phase. In the case of extending the sintering time to 30 minutes (Sample 4), the appearance of another phase from the Ni-Si system, *i.e.*, Ni_3Si, also called the mineral phase Carletonmooreite, was noted, with a simultaneous decrease in the share of the $Ni_{31}Si_{12}$ phase. Ni_3Si is formed in a wide temperature range (700 to 1035 °C), and it contains from 5 to 13.5 wt pct of silicon.[32] It crystallizes as the L12 fcc structure, and the determined unit cell lattice constant value is 3.537 Å, which is very close to the literature data (a = 3.51 Å).[33]

Slight changes in the lattice constant were also observed for the nickel matrix with an increase in the sintering time at 850 °C, from an initial value of 3.520 Å to 3.541 Å. This may indicate an increase in the volume of the unit cell, probably due to the incorporation of silicon atoms into the metallic nickel grains and the local formation of a nickel-silicon solid solution. For all analyzed samples sintered at 850 °C, presence of the carbon phase in the form of graphite in an amount not exceeding 1 pct was identified. The application of a higher sintering temperature (1000 °C) results in a similar range of changes occurring in a much shorter time (5 minutes). Finally, in both extreme cases (Sample 4 and Sample 6), the presence of silicon carbide was not identified, which confirms its complete decomposition.

C. *Raman Spectroscopy*

In line with the observations from previous techniques, we could expect a gradual degradation of the silicon carbide in the core and the appearance of free carbon and a new Ni-Si phase as a result. By examining the Raman spectrum in the range up to 1000 cm^{-1}, obtained in the above-described measurement conditions, it is possible to observe the presence of silicon carbide phonon modes. In the case of Sample 1, within the core, peaks around 776, 796, and 964 cm^{-1} are present, which indicates the presence of silicon carbide[34] [Figure 4(a) point A, (b)]. The silicon carbide modes are not observed outside the core region [Figure 4(a), point B, (b)]. Observing the spectrum in the range of 1400 to 2800 cm^{-1}, second-order modes of silicon carbide are visible in the area of the core (point A of Sample 1). At the shell of Sample 1, the SiC modes are not present, while three new modes appear near 1400, 1600, and 2700 cm^{-1} related to the presence of
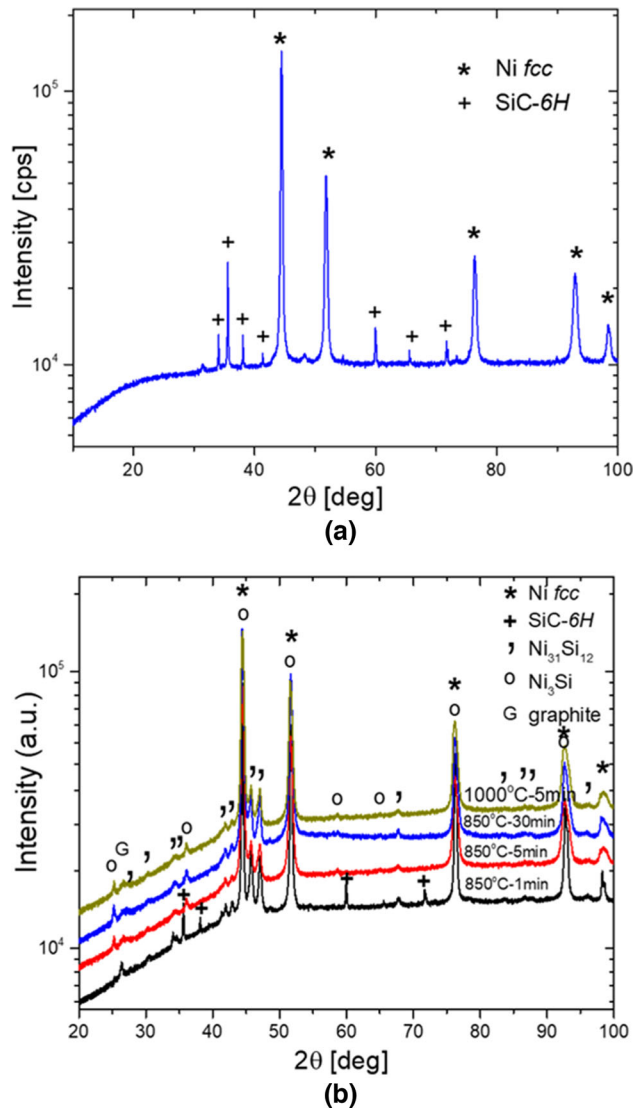
Fig. 3—XRD diffractograms of Ni-SiC composites at different stages of the sintering process: (*a*) starting material (Ni-SiC powder mixture), (*b*) sintered composites (Sample 1/2/4/6) (Color figure online).

carbon. Moreover, a mode close to 2700 cm^{-1}[35] indicates the presence of carbon organized into a hexagonal structure (graphite).

In the remaining cases, the presence of silicon carbide was not detected in any of the regions (Figures 5, 6). There are no modes in the spectral range up to 1000 cm^{-1}. On the other hand, the presence of graphite can be found in each of the tested points (both points A and B, *i.e.*, in the core and the shell) of Samples 4 and 6 [Figures 12(b) and 13(b)].

Based on the Raman observations, it can be concluded that after a 1-minute sintering process at 850 °C and 50 MPa (Sample 1), the presence of silicon carbide in the core of the composite is still noticeable, while carbon in the form of graphite is only found in the individual's envelope. For processes with an extended sintering process time of up to 30 minutes (Sample 4) or with an increased temperature of up to 1000 °C (Sample

6), the trace of silicon carbide disappears, while the presence of carbon in the form of graphite is noticeable throughout the entire area of the composite.

D. *Scanning Electron Microscopy*

The surface of the samples was imaged using a quadrant backscattered electron detector (QBSD) to reveal the morphology and the mass contrast of the elements, simultaneously. Looking at the SEM images, two main components were identified in the structure [Figures 7(a) and (b)]; black areas represent rest silicon carbide, and the light gray colour is directly correlated to the nickel matrix. Detailed analyses of the microstructure revealed the presence of additional phases characterized by intermediate shades of gray, which should be interpreted as the areas with a variable content of the main elements of the chemical composition.

Figure 7 shows the typical images of the microstructure for selected intermediate sintering stages of the Ni-SiC composite material. Each of the presented sample morphologies has a different structure and distribution of elements. As reported earlier,[17] above 500 °C, the reaction between nickel and silicon carbide occurs. In the case of sintering at 850 °C with a very short time of temperature exposure (Sample 1), the significant changes in the Ni/SiC interface area were observed. Within a few minutes, the decomposition of all visible SiC grains is noticed. In many cases, the reaction between the composite components occurs in the full range. The original SiC phase can be identified only within several larger grains. It means that the decomposition process occurs rapidly. The somewhat high densification degree at this stage of sintering allows for the interaction between the components. The nickel grains directly adjacent to SiC are the unlimited source of Ni atoms. With the extended time of sintering, the full consumption of the silicon carbide particles was observed [*e.g.,* Sample 3—Figures 7(c) and (d)]. In this case, the time of annealing at the maximum temperature was 15 times extended compared to Sample 1. Within the individual reinforcing areas, at least two different contrasts can be distinguished, which indicates the formation of new phases (Ni-Si) with variable elemental content. Additionally, some black inclusions appeared in the transformed areas, which suggests the formation of free carbon areas.

In the extreme case (Sample 6), the accumulation of the precipitates in the matrix/reinforcement boundary was noticed. A uniform contrast within the residual area after the SiC grains indicate the phase homogenization of the Ni-Si system. In this case the time needed to full SiC decomposition and formation of new phases is shorter due to the higher temperature of sintering process.

The microstructure and chemical composition was analyzed using the EDX method (energy dispersive X-ray spectroscopy) to determine the percentage of atoms of the main elements for the chosen sintered materials. The quantitative analysis of the chemical composition along the line through the interior, intermediate, and matrix area of Samples 1, 3, and 5 are
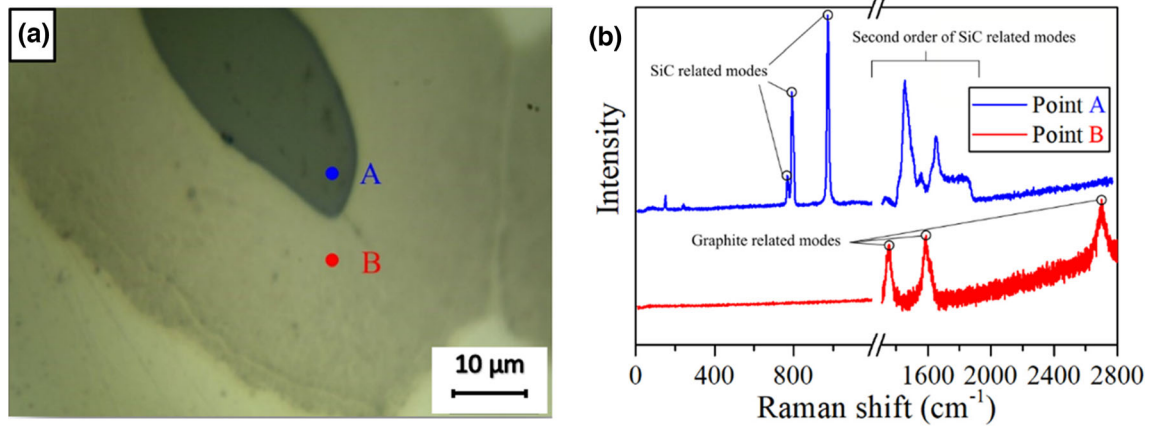
Fig. 4—Optical preview of Sample 1 with the indication of the spectral collection points (*a*) and the corresponding Raman spectra (*b*) (Color figure online).
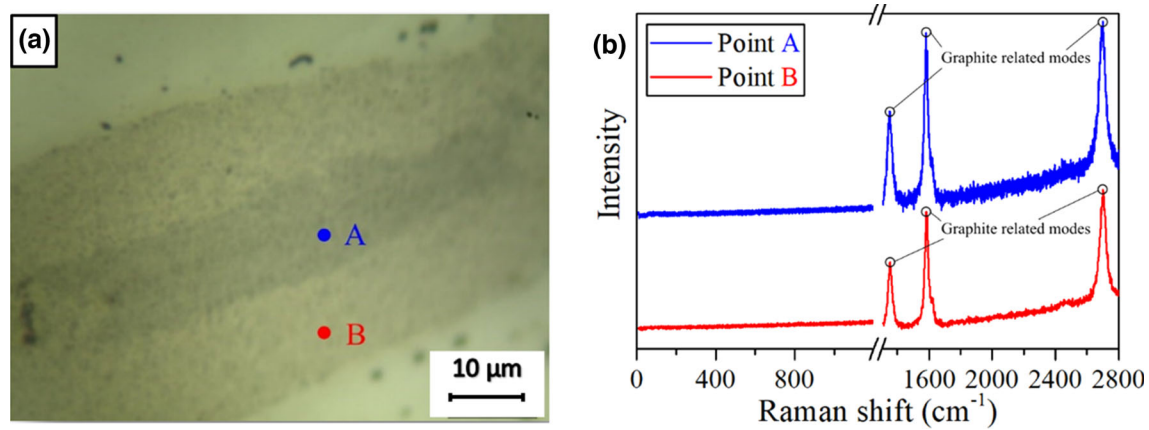

Fig. 5—Optical preview of Sample 4 with the indication of the spectral collection points (*a*) and the corresponding Raman spectra (*b*) (Color figure online).
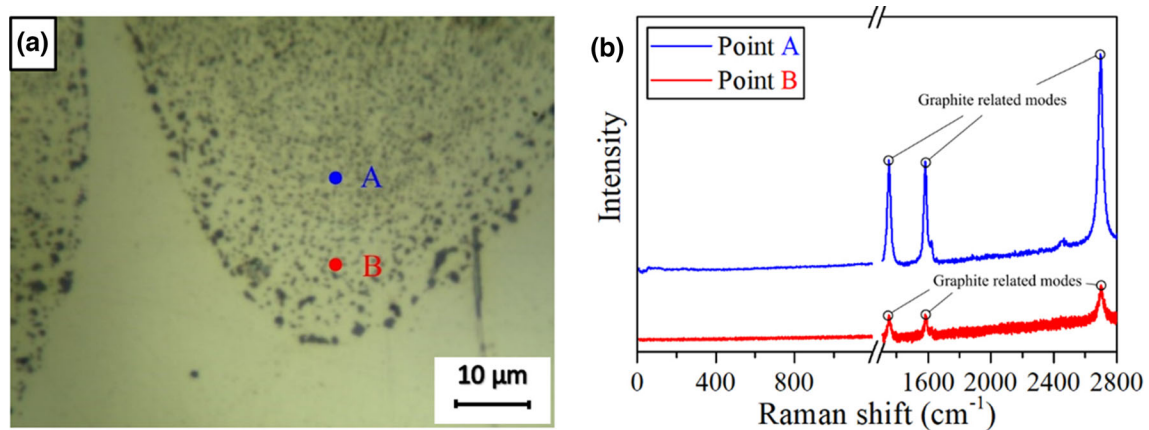

Fig. 6—Optical preview of Sample 6 with the indication of the spectral collection points (*a*) and the corresponding Raman spectra (*b*) (Color figure online).

shown in Figure 8. The elements present in the tested samples, C, Si, and Ni, are defined by red, green, and blue lines, respectively. Their distribution and the percentage of atomic content (the average due to the heterogeneity of the material and the spread of the result) are strictly dependent on the area of the measurement. Below the diagram of the distribution of elements, a fragment of the SEM image is shown with
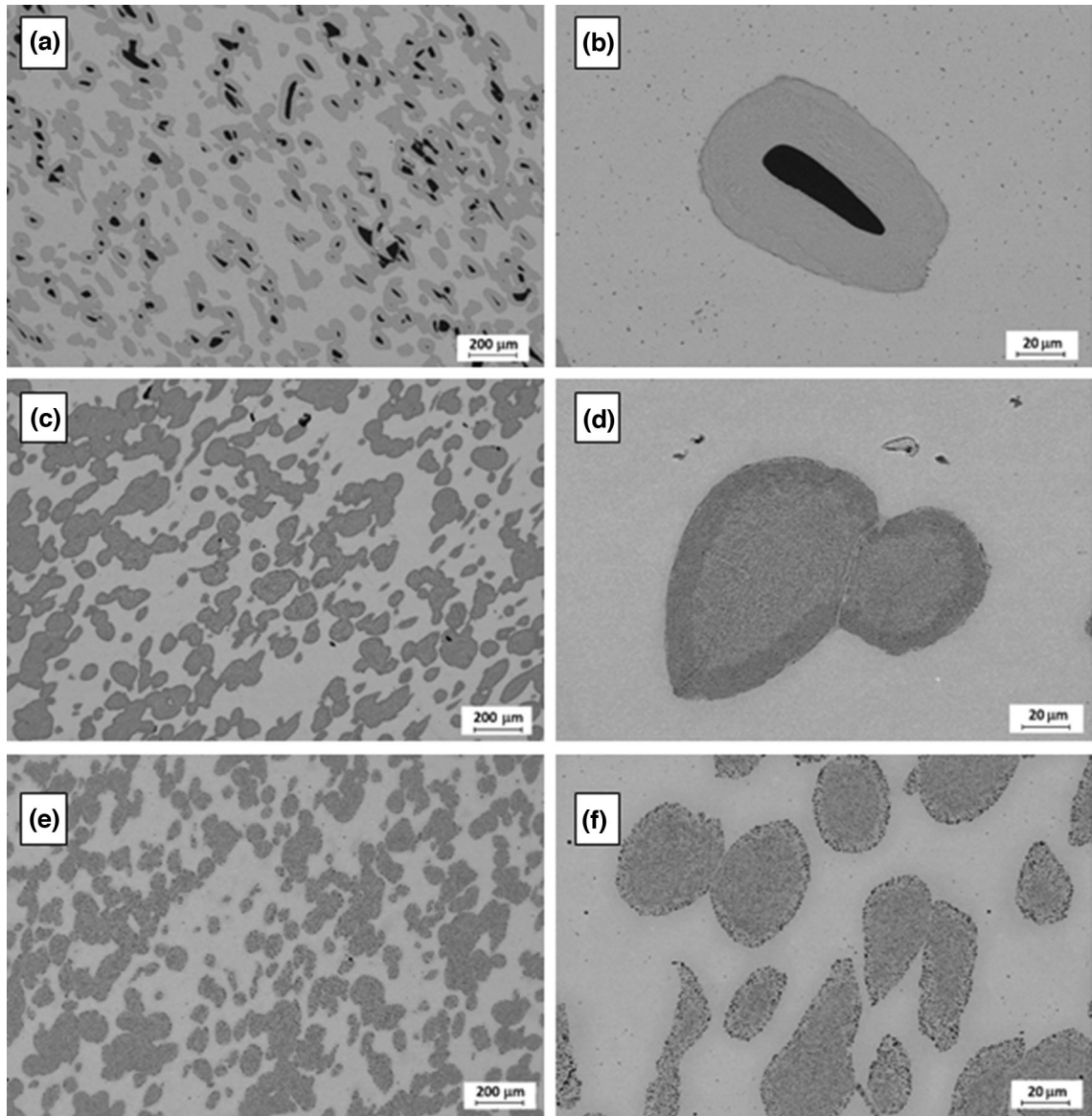
Fig. 7—SEM images of the Ni-SiC composite sintered at the following conditions: (*a*, *b*) Sample 1 (sintering temperature of 850 °C, sintering time of 1 minute, pressure of 50 MPa), (*c*, *d*) Sample 3 (sintering temperature of 850 °C, sintering time of 15 minutes, pressure of 50 MPa), (*e*, *f*) Sample 6 (sintering temperature of 1000 °C, sintering time of 5 minutes, pressure of 50 MPa).

the position of the line along which the EDX analysis was carried out marked. The concentration of elements gradually changes with the analysed line.

The analysis of the results of the quantitative measurement of the chemical composition confirmed that the inside of the grains of Sample 1 is a SiC material, while its shell is made of the following components: 25 at pct C, 20 at pct Si, 55 at pct Ni. The matrix is formed by the Ni element. In the case of the analysis of Sample 5, the following results were obtained: the grain interior is a heterogeneous structure with an average composition of 35 at pct C, 15 at pct Si, and 50 at pct Ni. The line of analysis passes through a narrow shell (32 to 37 μm on the distance axis) with the following composition: 50 at pct C, 10 at pct Si, 40 at pct Ni. It indicates the presence of the carbon-rich phase or carbon

precipitates in the Si-Ni matrix. It confirmed the homogenization of the Ni-Si system with the progress of sintering and, simultaneously, the migration of C precipitates to the matrix/reinforcement boundary.

The presented results of the chemical composition along the line show that the structure of the materials is heterogeneous at the early stages of sintering. Extension of the sintering time results in a uniform chemical composition in the transformed area. In order to obtain more unambiguous values of the percentage of the chemical composition, point EDX measurements were made in strictly defined, characteristic areas of the samples (grains and matrix). The SEM images with marked measurement points and the corresponding tables with numerical values of the percentage of elements are presented in Figure 9.
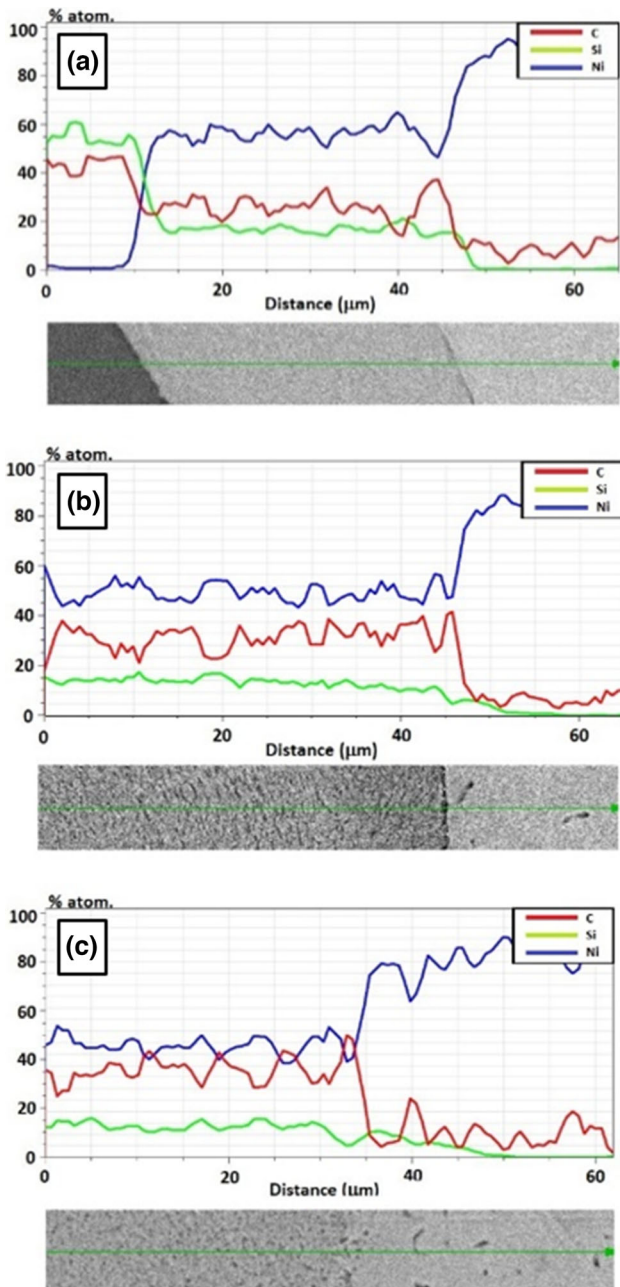
Fig. 8—EDX linear distribution of elements (Ni, C, Si) across the Ni-SiC interface: (a) Sample 1, (b) Sample 3, (c) Sample 5 (Color figure online).

Point quantitative analysis of the chemical composition of Samples 1, 4, and 6 consisted of making at least one measurement in each of the characteristic areas of the sample, i.e., in the area of the grain interior, on its shell structure, on the interface between the phases, and within the matrix. Examples of the results of the atomic content are presented in Tables in Figure 9. The list includes all the elements detected (the detection threshold < 1 at pct), including contaminants such as oxygen and carbon whose amounts can be disturbed by its presence in the cleaning agents.

Sample 1 has grains with a pure SiC core, as evidenced by the nearly 50 to 50 at pct share of C and Si elements. The shell, i.e., the transformed material around the SiC grain, is a heterogeneous material with a slightly different content of C, Si, and Ni. This heterogeneity is confirmed by SEM imaging at high magnification of the examined surface area. The boundary between nickel matrix and the interphase is clearly visible and the detailed measurement did not show an increase in at pct of either C or Si.

In the case of Sample 4, the SiC grains have completely decomposed, and the interior area of the transformed grain consists of very small carbon precipitates and phases from the Ni-Si system. The volumetric resolution of the EDX spot measurements does not allow for precise determination of the composition of individual phases; it can only provide average values. The conducted research shows that this area was significantly depleted by the Si element, and slightly larger dispersions of the at pct Ni content are revealed. A clearly distinguished shell is characterized by a slightly changed atomic composition of the elements, while the proportion of Ni and Si is definitely increased. It was observed that the closer to the interface between the matrix and reinforcement, the more carbon content is present in the composite structure.

In the case of Sample 6, the reactive zone is the most homogeneous globally, but locally, large carbon-rich precipitates are clearly visible. The inner area of the grain is the most rich in Si (about 8 pct). The shell area is practically free of Si and consists of carbon precipitates in the Ni matrix, while Si also appears outside the analyzed grain in the Ni matrix, in direct advancement to the grain. This may indicate its further dissolution in the nickel matrix of the composite occurring at the final stage of sintering.

E. Transmission Electron Microscopy Analysis

The detailed STEM/TEM investigation of the interface between nickel and silicon carbide particles is presented in Figures 10 and 11 for composites manufactured in various conditions. The structure of Sample 1 is presented in Figure 10 (performed by STEM) and 11 (performed by TEM + STEM). As confirmed by microstructural SEM investigation, Sample 1 can be characterized by the presence of three main zones: SiC ceramic reinforcement, interphase zone, and nickel matrix. Figure 10 presents an image carried out with high-angle annular dark field (HAADF), wherein the contrast is mostly based on the atomic number (Z-contrast). Hence, the Ni matrix indicates a bright color because it is composed of the heaviest elements among the components, while SiC appears as a dark area because it is the lightest component.

The most intriguing feature is related to the interphase zone, which is divided into two subphases [Figures 10(a) and 11(a)]. Both of them consist of nanoparticles/precipitations embedded in an interphase matrix, which in general can be treated as the multicomponent domain. The precipitations have sizes between 100 to 300 nm, and their highest concentration
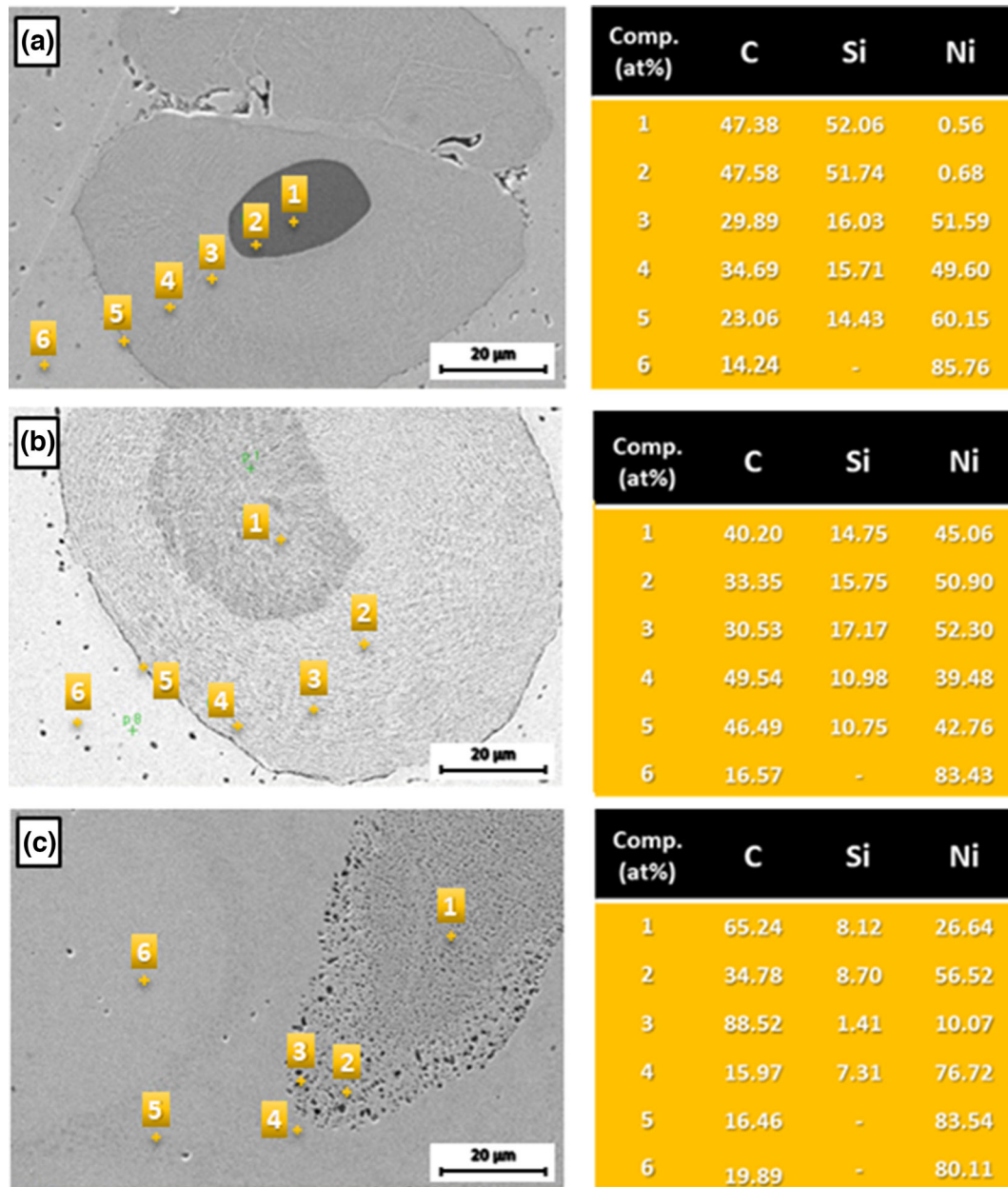
(a) Comp. (at%)	C	Si	Ni
1	47.38	52.06	0.56
2	47.58	51.74	0.68
3	29.89	16.03	51.59
4	34.69	15.71	49.60
5	23.06	14.43	60.15
6	14.24	-	85.76

(b) Comp. (at%)	C	Si	Ni
1	40.20	14.75	45.06
2	33.35	15.75	50.90
3	30.53	17.17	52.30
4	49.54	10.98	39.48
5	46.49	10.75	42.76
6	16.57	-	83.43

(c) Comp. (at%)	C	Si	Ni
1	65.24	8.12	26.64
2	34.78	8.70	56.52
3	88.52	1.41	10.07
4	15.97	7.31	76.72
5	16.46	-	83.54
6	19.89	-	80.11

Fig. 9—EDX points quantitative analysis of elements (Ni, C, Si): (*a*) Sample 1, (*b*) Sample 4, (*c*) Sample 6 (Color figure online).

can be observed near SiC particles (subphase 1). The precipitation content decreases with distance from the ceramic reinforcement (subphase 2). The EDX analysis reveals the high carbon content within the precipitations [Figure 10(c)]. Such a fact brought us to the conclusion that the carbon precipitations should be treated as the residual microstructural product after the dissolution of SiC particles with the nickel matrix.

Apart from the various concentrations of the carbon precipitations in both subphases, the different grain structures of the interphase matrix can also be shown. The first one, located within subphase I, is composed of fine grains with a diameter between 0.5 and 1.5 μm, whereas in the second one (subphase II), the grains are several microns in diameter, close to the pure nickel

ones. SAED images [Figure 11(a)] taken from this interphase zone confirms the intensive grain refinement of the matrix of subphase I (presence of almost full diffraction rings) and larger grains of subphase 2.

It should be noticed that subphase I is the first direct reaction product between Ni and SiC. Next, due to the nickel atoms diffusion, subphase II is formed. It can be assumed that the recrystallization process is responsible for grain growth in subphase II. It should be associated with the fact that subphase I is transformed to subphase II during the solid-state sintering. The sequence of product reaction was confirmed by the authors of[36] which is related to a higher diffusion rate of Ni than that of Si.[15] Furthermore, the analogical situation has been found in the paper of Shi *et al.*[37] concerning the SiC

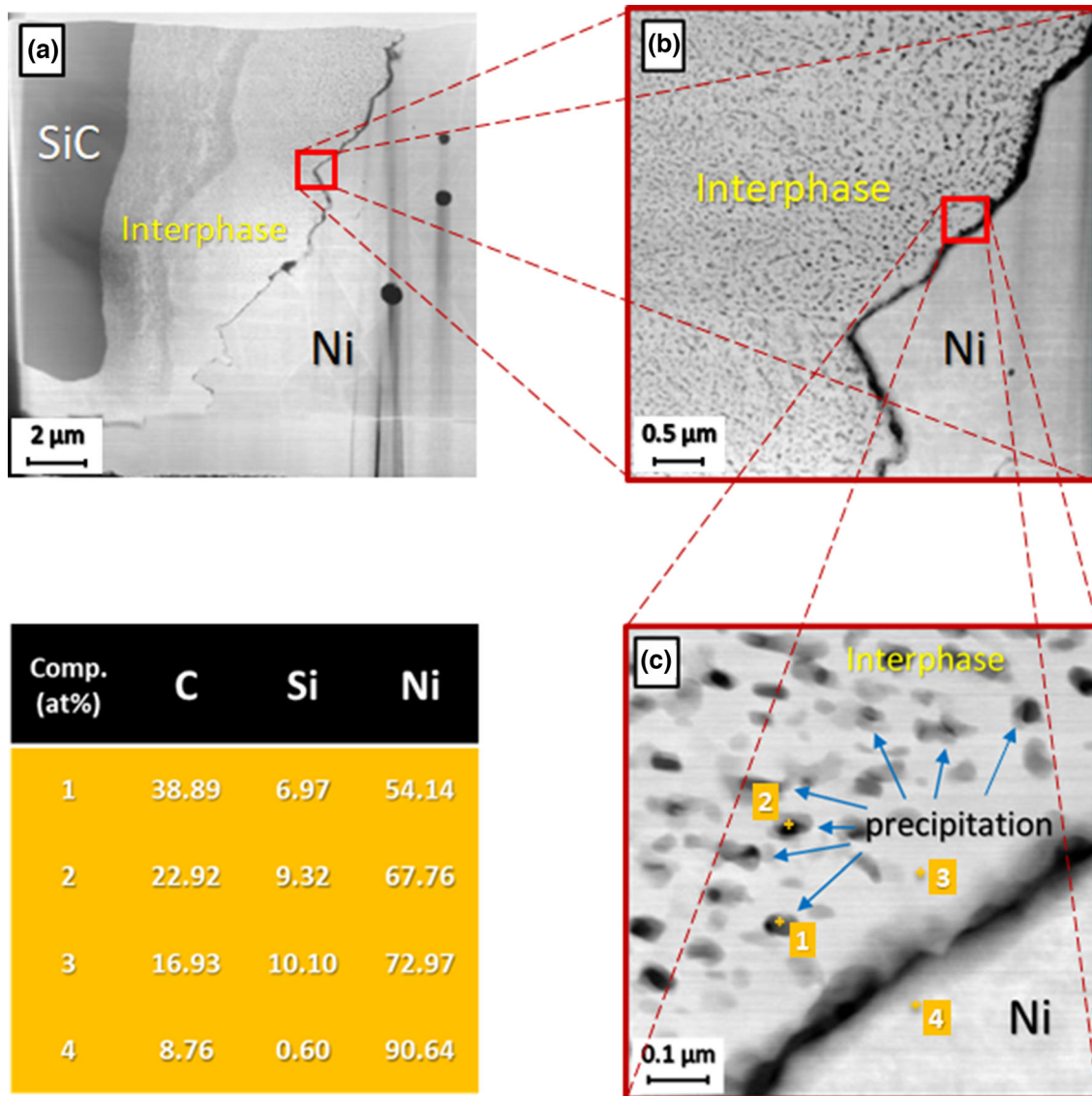| Comp. (at%)	C	Si	Ni
1	38.89	6.97	54.14
2	22.92	9.32	67.76
3	16.93	10.10	72.97
4	8.76	0.60	90.64

Fig. 10—STEM (HAADF mode) investigation of the Ni-SiC microstructure (Sample 1) with EDX analysis (Color figure online).

joints by pure nickel foil. It revealed a two-subphase structure with fine grains close to the SiC and larger ones near the pure nickel.

Furthermore, for both cases of the interphase matrix, the crystallographic features have been calculated to identify the specific phase of each subzone. As presented in Figure 11(a), subzone I indicates the combination of the crystallographic structure consisting of $Ni_{31}Si_{21}$, Ni_3Si, and Ni phases. The second subzone reveals mostly the $Ni_{31}Si_{21}$ phase. Finally, the SAED investigation from both subzones suggests that part of the material has an amorphous structure (blurred halo in the central region of the diffractogram). Such a feature should be connected with the presence of carbon nanoprecipitations within the multicomponent interphase zone.

Based on Figures 10 and 11, an ambiguous and heterogeneous character of the boundary condition of the interphase zone and nickel matrix can be observed.

The HAADF image reveals the serious discontinuity of the interface, which is clearly shown in Figure 10(c) in the high magnification. On the other hand, the TEM image (Figure 11) made from different spots discloses the high concentration of the carbon element within the interface zone (brighter color) observed as the layer with a width of approximately 50 nm. The migration of carbon to the boundary of the nickel matrix was confirmed by the linear EDX analysis [Figure 11(b)] manifested by the substantial peak of the C content in the interfacial spot comparable to those passing through carbon nanoprecipitations (*i.e.*, at the beginning of the EDX line). Both effects of the high carbon content and the local occurrence of discontinuities at the interface seem to be consistent with each other. Because the excessive carbon concentration stiffens the boundary, it induces significant states of residual stresses during the cooling process. As a consequence, it may cause several
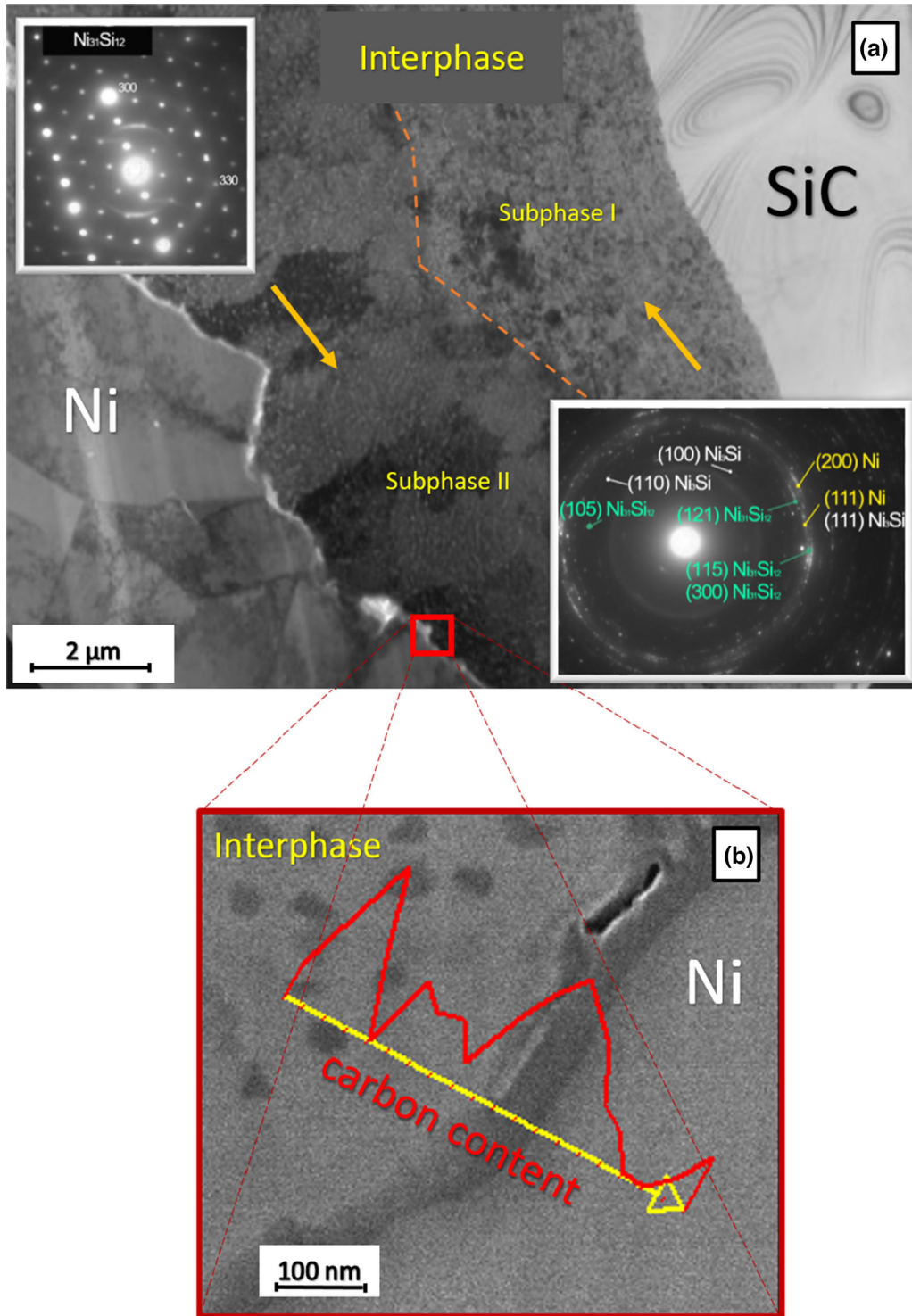
Fig. 11—Grains structure of Ni-SiC (Sample 1) performed by TEM (*a*) and STEM wih EDX analysis regarding the carbon content along the interface between the nickel and multicomponent interphase (*b*) (Color figure online).

structural defects (cracks, *etc*.) in the area of such a brittle layer.

Despite the minor differences presented in Figure 12, the structure of Sample 4 can be characterized in a similar way as Sample 1. The main distinction is related to the absence of the initial SiC particle, which completely dissolved in the Ni matrix and formed the interphase zone similar to those of Sample 1. In this case, the interphase is rather homogenous with the occurrence of a single subphase. Still, the interphase
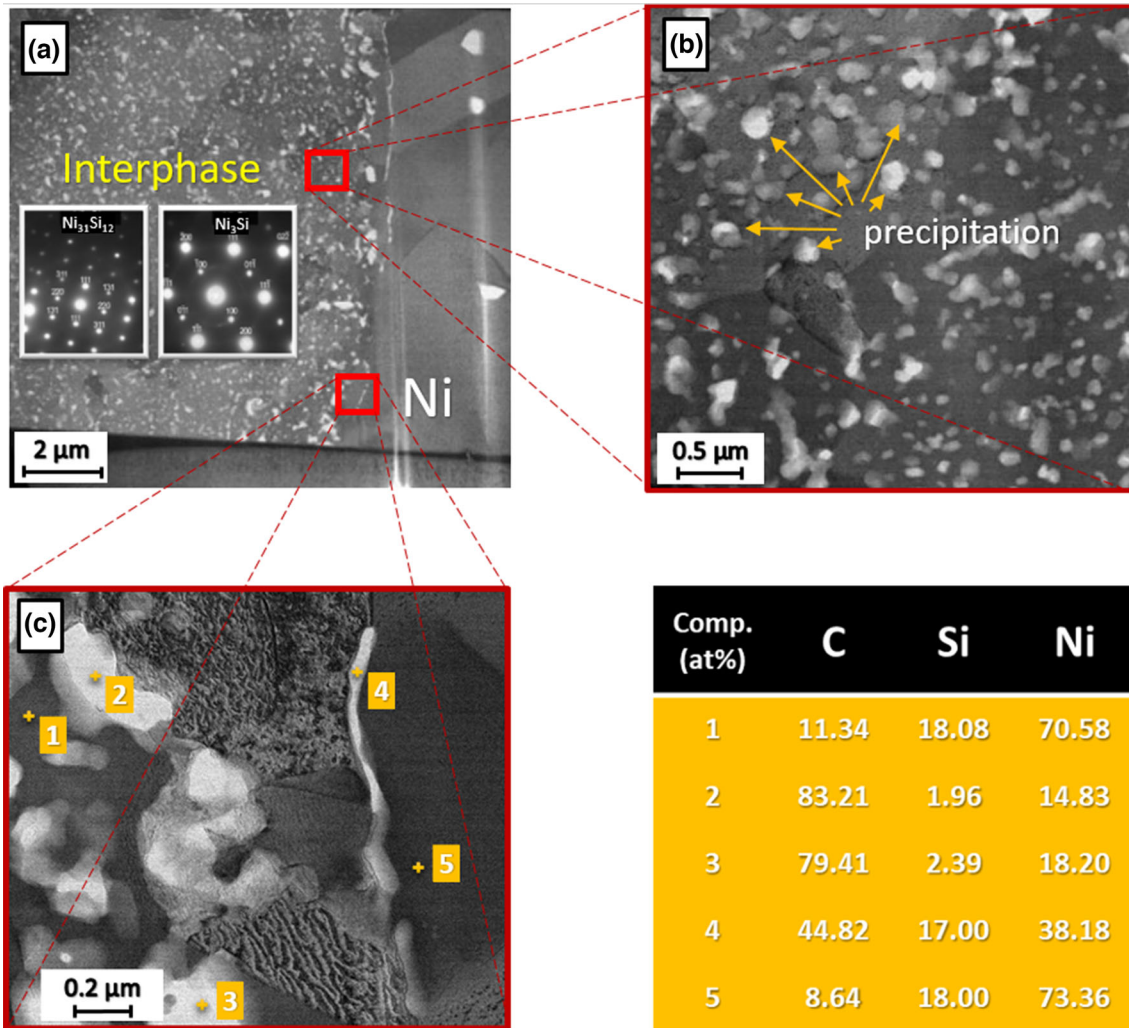
Fig. 12—STEM investigation of the Ni-SiC microstructure (Sample 4) with additional SAED and EDX analysis (Color figure online).
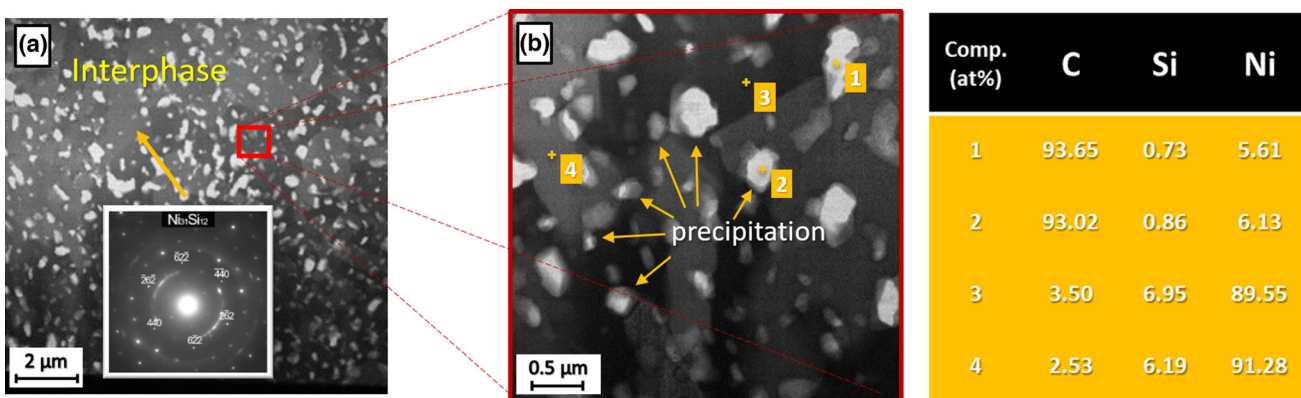
Comp. (at%)	C	Si	Ni
1	11.34	18.08	70.58
2	83.21	1.96	14.83
3	79.41	2.39	18.20
4	44.82	17.00	38.18
5	8.64	18.00	73.36

Fig. 13—STEM investigation of the Ni-SiC microstructure (Sample 6) with EDX and SAED analysis (Color figure online).

Comp. (at%)	C	Si	Ni
1	93.65	0.73	5.61
2	93.02	0.86	6.13
3	3.50	6.95	89.55
4	2.53	6.19	91.28

indicates the multi-component nature—the Ni silicide matrix with homogenously distributed carbon precipitations. One can observe that they have bigger diameters than those formed in Sample 1 (300 to 500 nm). It can be explained by the further and more profound migration of carbon from the completely dissolved SiC particle to nanoprecipitations. Analogously, the higher C content has been found in the interface of the Ni silicide–C interphase and pure nickel matrix [Figure 8(c)]. However, due to the longer sintering time,

no discontinuities, pores, or any defects have been revealed. The nickel silicide matrix in Sample 4 has an approximated grain size [Figure 8(a)] as the rest of the Ni matrix. Its phase composition consists of a mixture of $Ni_{31}Si_{21}$ and Ni_3Si phases, which has been obtained by SAED [Figure 12(a)].

In Sample 6 (Figure 13), similar to Sample 4, no central SiC particle can be observed. The structure of the interphase seems to be more homogenous compared to previous samples. The size of the amorphous nano-precipitations increases when compared with Sample 4 (the size of the nanoparticles varies between 400 and 700 nm). The structure of the interphase matrix [the single $Ni_{31}Si_{21}$ phase evaluated by SAED—Figure 13(a)] has also developed, and the grain size varies between 2 and 5 μm.

IV. DISCUSSION

Due to the fact that there are almost no literature references concerning the densification of Ni-SiC composite materials *via* the SPS method, our original results should be discussed in relation to other available techniques used. The only paper,[38] where authors used Spark Plasma Sintering to densify Ni-SiC is concentrated on the mechanical milling process on the reinforcement distribution in the metallic matrix. In the case of using SiC nanoparticles, no phase changes after sintering at 1150 °C for 30 minutes were reported. In the most cases, the investigations are performed for nickel-silicon thin films system.[34,35] According to the reported data, the microstructural changes at the nickel-silicon carbide interface starts after exceeding a temperature of about 500 °C.[39] On the direct contact area, the solid-state reaction between Ni and SiC occurs. Due to the nine silicides forming in the Ni-Si system, there is a variety of possible combinations of the final products. The decisive role in creating the final microstructure morphology and structure composition play the conditions of formation process, *e.g.,* reaction temperature, time of annealing, atmosphere, external load, *etc*. Several reports have been dedicated to the analyses of microstructural and phase changes in correlation to the process parameters. The analytical investigation devoted to the possible course of reaction based on the estimation of the Gibb's energies indicated that the most commonly formed phases are $NiSi_2$, $NiSi$, and Ni_2Si.[37,40]

In our investigation, the SPS method has been used to manufacture bulk Ni-SiC composites. It is a relatively new method of materials densification, but it is used more and more frequently due to numerous advantages. In particular, the limitation of the possible grain growth due to the lower sintering temperature, higher heating rate, and shorter sintering time in comparison to other methods makes it more and more popular.[36,41,42] We modified the process conditions to observe the microstructure and phase evolution of the sintered material. It should be emphasized that the relative density of the material is comparable (except for Sample 5, sintered in lower pressure assistance), which was the goal of the experiments, but the structure is significantly different. This diversity has a crucial effect on the macroscopic properties (*e.g.,* mechanical or thermal). The observed changes were very dynamic despite the very short time in the maximum sintering temperature. The transformation process occurring in the microstructure during sintering can be divided into specific stages:

- decomposition of silicon carbide in the contact of nickel,
- forming of a solid-state solution and then the creation of new nickel silicade phases,
- nucleations of carbon precipitates and their migration to the outer border between the pure nickel and nickel silicades.

With the appearance of new Ni-SiC contact surfaces, the decomposition reaction of silicon carbide takes place rapidly [Figure 7(a)]. This early stage continues until the ceramic phase is completely consumed [Figure 7(c)]. It should be noticed that the total time of SiC decomposition last only a few minutes when the global sample temperature does not exceed 850 °C. Due to the specific nature of the SPS process, the local temperature increase in the contact points of individual grains may appear, and additionally, the flow of electric current may accelerate the diffusion of atoms. After 1 minute sintering at 850 °C, a reactive zone covering tens of microns appeared and two subphases can be distinguished (Sample 1—Figure 11). It confirms that the front of the reaction moves very quickly to the center of the SiC grains and a new structure is formed. The morphology of the as-reacted material is not uniform at this stage. At the beginning, the amorphous structure of the Ni-Si solid solution is formed due to the diffusion and incorporation of silicon atoms into the nickel crystallographic unit. This is evidenced by a slight shift of the peaks representing nickel from their nominal positions (Figure 3). At the same time, the polycrystalline structures of $Ni_{31}Si_{12}$ and Ni_3Si are detected by the detailed TEM analyses. It should be noticed that range of the reactive zone in Sample 1 does not exceed 10 μm, and due to this fact, it was not confirmed by the XRD results. At the interphase, small amounts of nickel are present (subphase I—Figure 11) to support the further decomposition of the rest of the silicon carbide. The appearance of the amorphous material was reported by Rao *et al.*[43] where a high dose of Si ions during the implantation process of the Ni substrate caused its partial amorphization. Further annealing at temperatures exceeding 600 °C caused the crystallization of the Ni_3Si phase. As it was reported in,[43] the good crystallinity of Ni_3Si and good alignment to the nickel substrate was observed. On the other hand α-Ni-Ni_3Si eutectic irradiated with Ni-ions and annealed at 620 °C can be transformed to the $Ni_{31}Si_{12}$ intermetallic phase of the hexagonal structure.[44] In our investigation, the appearance of the amorphous structure at the beginning of interphase transformation can be caused by the current flowing across the material (similar effect to the ion implantation), but with further annealing, a fully crystalline structure is formed. Similarly, in[45] the
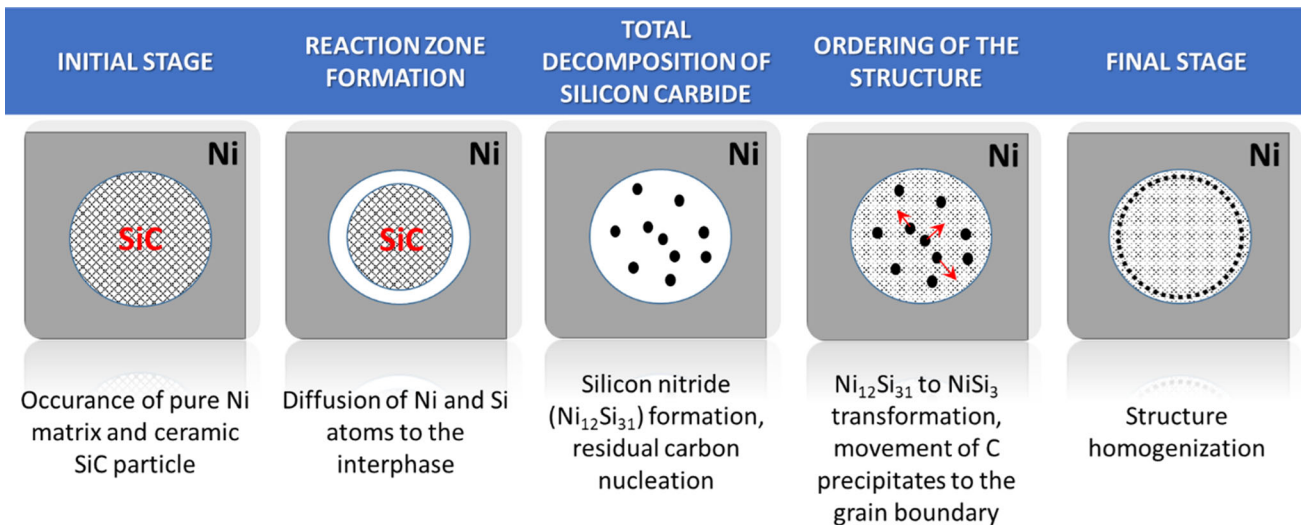
INITIAL STAGE	REACTION ZONE FORMATION	TOTAL DECOMPOSITION OF SILICON CARBIDE	ORDERING OF THE STRUCTURE	FINAL STAGE
Occurance of pure Ni matrix and ceramic SiC particle	Diffusion of Ni and Si atoms to the interphase	Silicon nitride $(Ni_{12}Si_{31})$ formation, residual carbon nucleation	$Ni_{12}Si_{31}$ to $NiSi_3$ transformation, movement of C precipitates to the grain boundary	Structure homogenization

Fig. 14—Schematic illustration of the microstructure evolution of Ni-SiC material during sintering *via* the SPS method.

original Ni-Si solid solution appears, which is then transformed subsequentially to Ni_3Si, $Ni_{31}Si_{12}$ to finally Ni_2Si phase. This phenomenon occurred after 1 minute of annealing at 550 °C, but the range of observed changes is about 100 nm. In our case, the range of observed changes is significantly larger after 1 minute of sintering in comparison to the results presented in.[45]

The observed silicon carbide decomposition process is very dynamic. It can be attributed to the phenomenon accompanying the SPS method. The effect of the solid mutual diffusion could be caused by the occurrence of the strong potential gradient related to the electric field. The DC power supply that was used in the SPS equipment may intensify the effects of diffusion, especially in the case of conducive materials. Rudinsky *et al.*[46,47] performed the SPS sintering process for Cu-Ni to study the effect of the electric current on the progress of diffusion. They observed that there is a strong diffusion effect at temperatures over 950 °C. It was attributed to the loss of nickel ferromagnetism in the presence of the electric current at the tested temperatures. It is caused by the rearrangement of electrons in the structure of the nickel band and the increase in the conductivity band resulting from the application of the current, which causes the chemical potential repulsion between copper atoms and nickel clusters. In our case, the range of structural evolution is much greater, which can be caused by the increased movement of atoms due to the flow of the current.[48] The applied SiC particles with a size of 40 to 80 μm completely react in the SPS process within a few minutes. Moreover, the observed speed of the structural changes in the area of the SiC grains is determined only by the diffusion rate of atoms in the contact area. In the SPS technique, the stabilization of the temperature inside the SiC particle compared to the contact area of the two particles in contact takes place in just a few milliseconds.[49] In our investigation, the SiC particles finally disappeared with the extension of the sintering time (Sample 2 and Sample 3 with sintering times of 5

and 15 minutes, respectively). The formation of the $Ni_{31}Si_{12}$ compound is also in good agreement with the TEM investigation provided by Kwon *et al.*,[15] where $Ni_{31}Si_{12}$ phase was identified as the reaction product of nickel film deposited on the 6H-SiC substrate and heat-treated at 550 °C.

The evolution of the free carbon formation process, as a product of SiC decomposition, was also observed in our investigation. Carbon does not react with silicon and nickel and does not form a stable phase with them.[50] At the beginning of the sintering process, carbon is present in the reactive zone in a dispersed form as small single precipitates. Their size and amount increase as the SiC decomposition process progresses. The TEM analyses indicated the forms of carbon at the early stage of sintering: individual precipitates across the whole interphase area and a carbon layer at the boundary between the pure nickel and the interphase zone. It is in good agreement with the studies mentioned above,[15] which indicated the grouping of carbon precipitates in particles, its movement to the external surface from the reaction zone, and the final formation of the thin film of graphite. The explanation of such a behavior can be found in,[15] where the authors indicated that the location of free carbon layer at the grain boundary reduces the interfacial energy.

Finally, the described mechanisms of interfacial interaction at the nickel-silicon carbide boundary is presented in Figure 14.

The Raman spectroscopy results confirmed the presence of carbon in the form of graphite after the SPS process. Although the detailed analyses especially in the case of peak below 1400 cm^{-1} can indicated for the presence of amorphous carbon. Similar observation are presented by Lim *et al.*[40] who distinguished the presence of two forms of carbon, graphite (peak G—1580 cm^{-1}) and amorphous carbon (peak D—1355 cm^{-1}), based on the Raman spectroscopy. On the other hand, this mode may be related to the damage in the structure of the hexagons of carbon in graphite.[51,52] With the progress of

sintering, the intensity of the carbon peaks increases and the initial individual precipitates form more complex clusters (see Figures 4, 5 and 6). The TEM results confirmed their growth from an initial 100 nm (Sample 1) to even 700 nm (Sample 4). The SAED analysis indicated a partially amorphous structure, which can be related to the amorphization of carbon nanoprecipitates (see Figure 12). A similar effect has been reported by the authors of;[15] amorphous carbon layers were also detected.

External load plays significant role for the progress of materials densification during sintering process. It impacts the sintering mechanisms by intensifying the diffusion process and increasing the progress of sintering. Additionally, the external load allows for the easier regrouping of particles at the beginning and effects on speed of pore elimination processes in the final stage of sintering. In the case of Sample 5, where the load was at a low level (5 MPa), the residual porosity was about 20 pct. It was generally localized between the nickel particles in the area of concentrated SiC particles. Although the contact areas between adjacent grains were limited, almost all SiC particles were decomposed. The Ni-Si structure was not uniform, with visible precipitates of carbon appearing accidentally across the reactive zone.

During materials densification via the SPS method, many independent factors influence the sintering mechanisms. Besides the temperature, time, and external pressure, the flowing current can directly influence on diffusion processes. With the progress of sintering, the number of intergrain contacts increases, accelerating SiC decomposition and finally resulting in the ordering of the system within the silicide area. With the increasing sintering temperature and time, more thermodynamically stable phases appeared. In our case, the dominant phase was Ni_3Si (Sample 6). Lim et al.[40] revealed the transformation from the Ni_3Si_2 phase to only the Ni_2Si compound after 2 hours of annealing at 1050 °C. Local melting areas were identified after 6 hours heat treatment at 1100 °C, where Ni_3Si and Ni_5Si_2 phases were identified as the reaction products.[53,54] In contrast, only the presence of Ni_2Si was noticed for Ni/4H-SiC wafers after annealing at 700 to 1000 °C.[55] In the higher range of temperatures (1245 °C), Ni_2Si and Ni_5Si_2 were present in the structure after 60 minutes annealing time.[36,56] In our case, there was no evidence of the presence of a liquid phase, even in the case of an increased sintering temperature of up to 1000 °C (Sample 6). The final product composition is dependent on the amount of the decomposed silicon. In our case, 20 vol pct of silicon carbide allowed for the identification of two $Ni_{31}Si_{12}$ and Ni_3Si phases. It should be emphasized that all available silicon atoms have been bonded in the silicide phases, and the residual nickel remained in the materials in an unchanged form (Ni-fcc).

V. CONCLUSION

In the presented study, the interfacial reaction between nickel and silicon carbide occurring during the sintering process was examined. To the best of our knowledge, this is the first attempt to describe the microstructural and structural changes for Ni-SiC composites sintered via the SPS method. The mechanism of the Ni-SiC interfacial reaction course during sintering has been proposed. The significant role of the process condition (temperature, time, pressure) in the formation of new phases from the Ni-Si system was proved. In the case of sintering at a higher temperature (1000 °C) the observed structural changes occur more rapidly. Due to the worse contact between particular grains for composites sintered with lower pressure (5 MPa), the range of the changes is much lower. It also results in a high amount of porosity in the composite structure.

Based on provided investigation the following conclusion can be draw:

- the interfacial reaction between nickel and silicon carbide after only 1 minute of sintering at 850 °C was observed,
- total decomposition of SiC after 5 minutes sintering at 850 °C was stated,
- scanning and transmission electron microscopy, X-ray diffraction, and Raman spectroscopy revealed the material transformation in the reaction zone resulting in two silicides (Ni_3Si and $Ni_{31}Si_{12}$) formation,
- individual carbon precipitates nucleation, their growth in the form of graphite and next clustering at the nickel matrix/reactive zone boundary in the final stage was distinguished,
- future investigations should consider the mechanical properties analysis of Ni-SiC composites and next the protection of ceramic particles by e.g., covering of silicon carbide with a thin metallic non-reactive layer.[57]

CONFLICT OF INTEREST

On behalf of all authors, the corresponding author states that there is no conflict of interest.

OPEN ACCESS

REFERENCES

1. H. Tanaka: *J. Ceram. Soc. Jpn.*, 2011, vol. 119(3), pp. 218–33.
2. D.K.Q. Mu, Z. Zhang, Y.H. Xie, J.M. Liang, J. Wang, and D.L. Zhang: *Mater. Charact.*, 2021, vol. 175, p. 111090.
3. Y. Gu, M. Yi, Y. Chen, J. Tu, Z. Zhou, and J. Luo: *Mater. Charact.*, 2022, vol. 193, p. 112300.
4. Th. Schubert, B. Trindade, T. Weißgarber, and B. Kieback: *Mater. Sci. Eng. A*, 2008, vol. 475, pp. 39–44.
5. K.M. Rahman, V.A. Vorontsov, S.M. Flitcroftand, and D. Dye: *Adv. Eng. Mater.*, 2017, vol. 19(7), p. 1700027.
6. K. Mizuuchi, K. Inoue, Y. Agari, T. Nagaoka, M. Sugioka, M. Tanaka, T. Takeuchi, J. Tani, M. Kawahara, Y. Makino, and M. Ito: *Composites B*, 2012, vol. 43(4), pp. 2012–19.
7. F. Azarmi: *Composites B*, 2011, vol. 42(7), pp. 1779–85.
8. M. Masoudi, M. Hashim, H.M. Kamari, and M.S. Salit: *Appl. Nanosci.*, 2013, vol. 3, pp. 357–62.
9. Y.L. Dong, F.M. Xu, X.L. Shi, C. Zhang, Z.J. Zhang, J.M. Yang, and Y. Tan: *Mater. Sci. Eng. A*, 2009, vol. 504, pp. 49–54.
10. Y. Katoh, L.L. Snead, C.H. Henager Jr., T. Nozawa, T. Hinoki, A. Ivekovic, S. Novak, and S.M. Gonzalez de Vicente: *J. Nucl. Mater.*, 2014, vol. 455, pp. 387–97.
11. D.K. Bagal, B. Parida, A. Barua, B. Naik, S. Jeet, S.K. Singh, and A.K. Pattanaik: *IOP Conf. Ser.: Mater. Sci. Eng.*, 2020, vol. 970, p. 012017.
12. M. Kotani, T. Inoue, A. Kohyama, Y. Katoh, and K. Okamura: *Mater. Sci. Eng. A*, 2003, vol. 357, pp. 376–85.
13. D. Mao, X. Meng, Y. Xie, Y. Chang, Z. Qin, S. Xu, L. Wan, and Y. Huang: *Sci. China Mater.*, 2022, (in press).
14. L. Liu, H. Zhao, W. Hu, and B. Shen: *Mater. Lett.*, 2005, vol. 59, pp. 3014–17.
15. Y. Kwon, B.S. An, and C.W. Yang: *Mater. Charact.*, 2018, vol. 140, pp. 259–64.
16. S. Cichoň, P. Macháč, B. Barda, V. Machovič, and P. Slepička: *Thin Solid Films*, 2012, vol. 520, pp. 4378–88.
17. G. Gyawali, K. Hamal, B. Joshi, A. Rajbhandari, and S.W. Lee: *Mater. Lett.*, 2014, vol. 126, pp. 228–31.
18. J. Li, O. Lin, C. Cheng, W. Wang, C. Xu, and L. Ren: *J. Mater. Process. Technol.*, 2021, vol. 290, p. 116987.
19. A.F. Zimmerman, G. Palumbo, K.T. Aust, and U. Erb: *Mater. Sci. Eng. A*, 2002, vol. 328, pp. 137–46.
20. C. Yang, T. Wei, O. Muránsky, D. Carr, H. Huang, and X. Zhou: *Mater. Charact.*, 2018, vol. 138, pp. 289–95.
21. H. Wang, S. Yao, and S. Matsumura: *J. Mater. Process. Technol.*, 2004, vol. 145, pp. 299–302.
22. A.F. Zimmerman, D.G. Clark, K.T. Aust, and U. Er: *Mater. Lett.*, 2002, vol. 52, pp. 85–90.
23. A. Bachli, M.A. Nicolet, L. Baud, C. Jaussaud, and R. Madar: *Mater. Sci. Eng. B*, 1998, vol. 56, pp. 11–23.
24. Y. Cao and L. Nyborg: Contact formation on silicon carbide by use of nickel and tantalum from a materials science point of view, in *Properties and applications of silicon carbide*. IntechOpen, London, 2011, pp. 171–94.
25. R.M. German: *Sintering—theory and practice*, A Wiley-Interscience Publications, New York, 1996.
26. T. Fujimura and S.I. Tanaka: *J. Mater. Sci.*, 1999, vol. 34, pp. 235–39.
27. J.S. Park, K. Landry, and J.H. Perepezko: *Mater. Sci. Eng. A*, 1999, vol. 259, pp. 279–86.
28. A. Hahnel, E. Pippel, V. Ischenko, and J. Woltersdorf: *Mater. Chem. Phys.*, 2009, vol. 114, pp. 802–08.
29. S. Sanzaro, C. Bongiorno, P. Badalà, A. Bassi, I. Deretzis, M. Enachescu, G. Franco, G. Fisicaro, P. Vasquez, A. Alberti, and A. La Magna: *Materials (Basel)*, 2021, vol. 14(16), p. 4769.
30. J. Trapp and B. Kieback: *Powder Metall.*, 2019, vol. 62(5), pp. 297–306.
31. F. La Via, F. Roccaforte, A. Makhtari, V. Raineri, P. Musumeci, and L. Calcagno: *Microelectron. Eng.*, 2002, vol. 60, pp. 269–82.
32. M. Alizadeh and S. Narouei: *J. Alloys Compd.*, 2019, vol. 772, pp. 565–72.
33. A.T. Dutra, P.L. Ferrandini, and R. Caram: *J. Alloys Compd.*, 2007, vol. 432, pp. 167–71.
34. A. Mondon, M.N. Jawaid, J. Bartsch, M. Glatthaar, and S.W. Glunz: *Sol. Energy Mater. Sol. Cells*, 2013, vol. 117, pp. 209–13.
35. P.L. Tam, Y. Cao, U. Jelvestam, and L. Nyborg: *Surf. Coat. Technol.*, 2011, vol. 206(6), pp. 1160–67.
36. O. Guillon, J. Gonzalez-Julian, B. Dargatz, T. Kessel, G. Schierning, J. Rathel, and M. Herrmann: *Adv. Eng. Mater.*, 2014, vol. 16(7), pp. 830–49.
37. H. Shi, Y. Chai, N. Li, J. Yan, X. Zhu, K. Chen, D. Bai, Z. Liu, M. Wu, R. Zhang, M. Li, M. Luo, Q. Sun, C. Xin, W. Hu, and X. Dong: *J. Eur. Ceram. Soc.*, 2020, vol. 40, pp. 5162–71.
38. H. Huang, C. Yang, M. de los Reyes, Y. Zhou, L. Yan, and X. Zhou: *J. Mater. Sci. Technol.*, 2015, vol. 31(9), pp. 923–29.
39. E. Kurimoto, H. Harima, T. Toda, M. Sawada, M. Iwami, and S. Nakashima: *J. Appl. Phys.*, 2002, vol. 91, p. 10215.
40. C. Lim, H. Nickel, A. Naoumidis, and E. Gyarmati: *J. Mater. Sci.*, 1997, vol. 32, pp. 6567–72.
41. S. Nosewicz, P. Bazarnik, M. Clozel, Ł Kurpaska, P. Jenczyk, D. Jarząbek, M. Chmielewski, B. Romelczyk-Baishya, M. Lewandowska, Z. Pakieła, Y. Huang, and T.G. Langdon: *Arch. Civ. Mech. Eng.*, 2021, vol. 21, p. 131.
42. A. Flaureau, A. Weibel, G. Chevallier, and C. Estournes: *J. Eur. Ceram. Soc.*, 2021, vol. 41(6), pp. 3581–94.
43. Z. Rao, J.S. Wiliams, and D.K. Sood: *AIP J. Appl. Phys.*, 1993, vol. 74(7), pp. 4792–94.
44. C.A. Camacho-Olguin, A. Garcia-Borquez, V. Paz del Angel, J. Ascencion Montoya-De La Fuente, C.A. Gonzalez-Rodriguez, L.M. Ramos-Tercero, H. Cruz-Meija, and R.A. Rodriguez-Diaz: *Radiat. Eff. Defects Solids*, 2020, vol. 175(910), pp. 925–37.
45. S. Lim, J.S. Oh, Y. Kwon, B.S. An, J.H. Bae, T.H. Kim, M.H. Park, H.S. Kim, and C.W. Yang: *J. Nanosci. Nanotechnol.*, 2016, vol. 16, pp. 10853–57.
46. S. Rudinsky, E. Gauvin, and M. Brochu: *AIP J. Appl. Phys.*, 2014, vol. 116(15), p. 154901.
47. S. Rudinsky and M. Brochu: *Scripta Mater.*, 2015, vol. 100, pp. 74–7.
48. M. Abedi, A. Asadi, S. Vorotilo, and A.S. Mukasyan: *J. Mater. Sci.*, 2021, vol. 56, pp. 19739–66.
49. J. Trapp, A. Semenov, O. Eberhardt, M. Nöthe, T. Wallmersperger, and B. Kieback: *Powder Metall.*, 2020, vol. 63(5), pp. 312–28.
50. F. Goesmann and R. Schmid-Fetzer: *Mater. Sci. Eng. B*, 1997, vol. 46, pp. 357–62.
51. A. Pimenta, G. Dresselhaus, M.S. Dresselhaus, L.G. Cancado, A. Jorio, and R. Saito: *Phys. Chem. Chem. Phys*, 2007, vol. 9(11), pp. 1276–91.
52. S. Reich and C. Thomsen: *Philos. Trans. R. Soc. A*, 2004, vol. 362(1824), pp. 2271–88.
53. T.C. Chou, A. Joshi, and J. Wadsworth: *J. Vac. Sci. Technol. A*, 1991, vol. 9, pp. 1525–34.
54. H. Shi, Y. Chai, N. Li, J. Yan, H. Peng, R. Zhang, M. Li, D. Bai, K. Chen, Z. Liu, M. Luo, Q. Sun, X. Zhu, Y. Zhang, R. Li, B. Zhang, and X. Dong: *J. Eur. Ceram. Soc.*, 2021, vol. 41(7), pp. 3960–69.

55. J. Rogowski and A. Kubiak: *Mater. Sci. Eng. B*, 2012, vol. 177, pp. 1318–22.
56. H. Shi, H. Peng, Y. Chai, N. Li, Y. Wen, D. Bai, Z. Liu, J. Yan, R. Zhang, M. Li, K. Chen, M. Luo, Q. Sun, R. Li, and X. Dong: *J. Eur. Ceram. Soc.*, 2021, vol. 41(13), pp. 6238–47.
57. Q. Ge, M. Yan, Y. Jiang, Y. Wang, and J. Liu: *J. Superhard Mater.*, 2022, vol. 44(6), pp. 393–404.